



**POLITECNICO**  
MILANO 1863

SCUOLA DI INGEGNERIA INDUSTRIALE  
E DELL'INFORMAZIONE

EXECUTIVE SUMMARY OF THE THESIS

## Adaptive augmentation of Incremental NDI laws with systematic $\mathcal{H}_\infty$ tuning

LAUREA MAGISTRALE IN AERONAUTICAL ENGINEERING - INGEGNERIA AERONAUTICA

**Author:** GIULIO FRANCESCHINI

**Advisor:** PROF. DAVIDE INVERNIZZI

**Co-advisors:** GIOVANNI GOZZINI, PHD; GIORGIO RAOS, MSc

**Academic year:** 2024-2025

### Introduction

Control systems for drones and high-performance aircraft must address significant nonlinearities and uncertainties. Incremental Nonlinear Dynamic Inversion (INDI) is a promising framework due to its model-free structure and disturbance rejection capabilities. However, its sensitivity to noise, delays, and modeling errors hinders its industrial use and certification. This work aims to develop an adaptive INDI extension with systematic robust synthesis capabilities, thereby enabling formal verification and paving the way toward certifiable INDI flight control systems.

### 1. Incremental Nonlinear Dynamic Inversion

Incremental Nonlinear Dynamic Inversion (INDI) has recently gained significant attention in aerospace research. Its ability to incrementally adjust control inputs based on measured changes in system dynamics enables robust performance without requiring a precise model of the entire system [4] and reducing the need for gain scheduling.

Linearizing  $\dot{x} = f(x, u)$  around an operating point, one obtains

$$\dot{x} = f(x_0, u_0) + F(x_0, u_0) \Delta x + G(x_0, u_0) \Delta u.$$

By selecting the control law as

$$\Delta u = G(x_0, u_0)^{-1} [\nu - f(x_0, u_0)],$$

the closed-loop dynamics, under the assumption of fast actuators, is approximately equivalent to a pure integrator:

$$\dot{x}(t) = \nu(t).$$

The virtual input  $\nu$  can be designed using linear controllers.

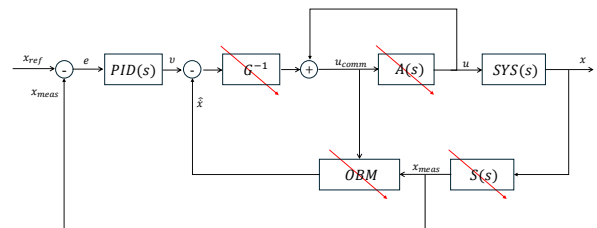


Figure 1: Typical INDI control loop with uncertainty sources indicated by red lines.

Practical limitations of INDI arise from the computation of the required derivative information  $\dot{x}_0 = f(x_0, u_0)$ . Sensor-based implementations suffer from phase lag and noise, whereas model-based designs introduce estimation errors [5]. Additional challenges stem from actuator saturation and inaccuracies in the control effectiveness  $G$ , as well as time delays and external disturbances (Figure 1). While embedding adaptive blocks in the INDI loop can mitigate some issues [2, 3], it complicates stability analysis and the use of classical robustness-analysis tools, making certification more challenging.

## 2. ESO augmentation and $\mathcal{H}_\infty$ synthesis

### 2.1. INDI under non-idealities

A control-affine nonlinear plant with uncertainties in dynamics and control effectiveness is described by

$$\dot{x} = f(x) + \Delta f(x) + (G(x) + \Delta G(x)) u.$$

As demonstrated in [1], the ideal model-based version of the INDI is equivalent to the classical NDI control law. It is therefore possible to study the effects of uncertainty by applying the NDI control law

$$u = G(x)^{-1}(\nu - f(x)),$$

which yields the perturbed integrator dynamics

$$\dot{x} = \nu + \Delta f(x) + \Delta G(x) G(x)^{-1}(\nu - f(x)).$$

By collecting all the perturbed terms into a single virtual disturbance

$$\sigma(t) = \Delta f(x) + \Delta G(x) G^{-1}(x)(\nu - f(x)),$$

the INDI loop reduces to

$$\dot{x}(t) = \nu(t) + \sigma(t).$$

To retrieve the ideal result of the INDI control law,  $\sigma(t)$  must be cancelled. The complex INDI non-ideal behavior is recast into a classical linear disturbance rejection problem (Figure 2). This result constitutes a considerable simplification compared to the  $\mathcal{L}_1$  approach [2], where uncertainties are remapped onto the actuators, thereby requiring a larger number of states in the adaptive controller.

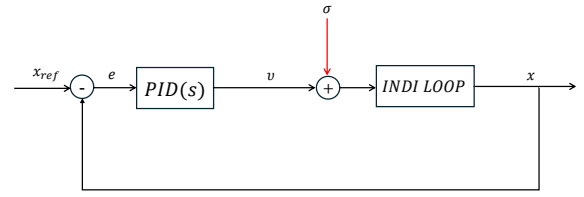


Figure 2: Simplified model of the non-ideal INDI.

### 2.2. ESO-based disturbance compensation

To reject the virtual disturbance  $\sigma(t)$ , an adaptive augmentation strategy is employed within the Predictive Model Reference Adaptive Control (PMRAC) framework. The virtual control input is augmented as

$$\nu(t) = \nu_{\text{bl}}(t) + \nu_{\text{ad}}(t),$$

where  $\nu_{\text{bl}}(t)$  is the baseline control component, and  $\nu_{\text{ad}}(t)$  is an adaptive contribution designed to cancel the disturbance  $\sigma(t)$ . This adaptive term is generated by a first-order Extended State Observer (ESO), which estimates both the system state and the lumped disturbance in real time. The ESO aims to produce an output  $\nu_{\text{ad}}(t)$  that is ideally equal and opposite to the disturbance, *i.e.*,  $\nu_{\text{ad}}(t) = -\sigma(t)$ , thereby recovering the nominal dynamics of the baseline controller. The observer reconstructs the disturbance from available measurements. Denoting the estimates by  $\hat{x}(t)$  and  $\hat{\sigma}(t)$ , and using observer gains  $L_1$  and  $L_2$ , the ESO dynamics are defined as:

$$\begin{aligned} \dot{\hat{x}}(t) &= \nu(t) + \hat{\sigma}(t) + L_1(x_{\text{meas}}(t) - \hat{x}(t)) \\ \dot{\hat{\sigma}}(t) &= L_2(x_{\text{meas}}(t) - \hat{x}(t)). \end{aligned}$$

The resulting control contribution is then:

$$\nu_{\text{ad}}(t) = -\hat{\sigma}(t).$$

As  $\hat{\sigma}(t)$  approaches  $\sigma(t)$ , the adaptive contribution  $\nu_{\text{ad}}(t) = -\hat{\sigma}(t)$  increasingly cancels the disturbance, thus restoring the ideal behavior dictated by the baseline controller.

Defining the estimation errors as  $\tilde{x} = x_{\text{meas}} - \hat{x}$ ,  $\tilde{\sigma} = \sigma - \hat{\sigma}$ , the error dynamics can be expressed as

$$\begin{bmatrix} \dot{\tilde{x}} \\ \dot{\tilde{\sigma}} \end{bmatrix} = \begin{bmatrix} -L_1 & I \\ -L_2 & 0 \end{bmatrix} \begin{bmatrix} \tilde{x} \\ \tilde{\sigma} \end{bmatrix}.$$

Selecting  $L_1, L_2$  so that this matrix is Hurwitz ensures  $\tilde{x}, \tilde{\sigma} \rightarrow 0$  and thus  $\dot{x} \rightarrow \nu_{\text{bl}}$ .

To bound the disturbance estimate and avoid the well-known issue of parameter drifting, a projection operator  $\text{Proj}_\Theta$  onto a convex set  $\Theta$  is applied. For a parameter estimate  $\theta(t) \in \Theta$ , the general adaptation law is

$$\dot{\theta}(t) = \text{Proj}_\Theta(\gamma e(t) \phi(x, t))$$

where  $\gamma$  is the adaptation gain and  $\phi$  is the regressor. In this case,  $\theta = \hat{\sigma}$ ,  $e = \tilde{\sigma}$ ,  $\gamma = L_2$  and  $\phi = 1$ . The projection is inactive inside  $\Theta$  and removes outward update components on  $\partial\Theta$ , thus ensuring boundedness.

### 2.3. Delay-aware ESO

To accommodate a control delay  $\Delta T$ , the ESO prediction uses a delayed virtual control:

$$\begin{aligned} \hat{x}(t) &= \nu(t - \Delta T) + \hat{\sigma}(t) + L_1(x_{\text{meas}}(t) - \hat{x}(t)) \\ \hat{\sigma}(t) &= L_2(x_{\text{meas}}(t) - \hat{x}(t)). \end{aligned}$$

This modification synchronizes observer predictions with the actual delayed input, improving robustness. Simulations show excellent performance (Figure 10) even in the absence of an exact delay model.

### 2.4. $\mathcal{H}_\infty$ tuning

The architecture is a linear feedback loop with an output disturbance, making it amenable to a structured  $\mathcal{H}_\infty$  synthesis. In the SISO case, five tuning parameters are available:

$$K_p, \quad K_i, \quad K_d, \quad L_1, \quad L_2,$$

where  $K_p, K_i, K_d$  are the proportional, integral, and derivative gains of the PID controller (Figure 4), and  $L_1, L_2$  are the ESO gains. Three frequency-domain performance specifications are imposed:

- *Tracking weight*: high loop gain at very low frequencies to eliminate steady-state error and moderate gain at low frequencies to ensure responsiveness while avoiding excessive bandwidth reduction.
- *Disturbance-rejection weight*: similar to the tracking weight, but extends toward the loop bandwidth to effectively counteract broad-spectrum virtual disturbances caused by INDI non-idealities.
- *Control-authority weight*: penalizes control authority moderately within the actuator bandwidth to prevent saturation, and imposes a sharp increase beyond.

Including sensor dynamics does not alter the tuning methodology; the same three weighting functions suffice for  $\mathcal{H}_\infty$  synthesis.

### 2.5. Final considerations

The proposed formulation reduces the INDI+adaptive design to the selection of three weighting functions, replacing manual gain adjustments with automated  $\mathcal{H}_\infty$  synthesis. The underlying loop remains linear without loss of generality, allowing for classical stability-margin analysis and facilitating certification and industrial deployment. Compared to previous adaptive INDI schemes, this approach offers a simplified and standardizable tuning procedure.

## 3. Case study: longitudinal autopilot

### 3.1. Aircraft model

A model for the longitudinal dynamics of an aircraft taken from [3] is used to test the developed control formulation. In the body-fixed frame, the general force and moment equilibrium are

$$\begin{aligned} \frac{d}{dt}(V_{\mathcal{I}/\mathcal{B}})^{\mathcal{B}} &= \frac{1}{m}(F_a^{\mathcal{B}} + F_g^{\mathcal{B}}) - (\omega_{\mathcal{I}/\mathcal{B}}^{\mathcal{B}}) \times (V_{\mathcal{I}/\mathcal{B}})^{\mathcal{B}} \\ \frac{d}{dt}(\omega_{\mathcal{I}/\mathcal{B}})^{\mathcal{B}} &= I_G^{-1} \left( M_a^{\mathcal{B}} - \omega_{\mathcal{I}/\mathcal{B}}^{\mathcal{B}} \times I_G \omega_{\mathcal{I}/\mathcal{B}}^{\mathcal{B}} \right). \end{aligned}$$

Under the assumption of mass distribution symmetry about the  $x$ - $z$  plane and classical aerodynamic decoupling, the control problem can be split into the longitudinal and lateral-directional motions. Focusing on the former, the plant can be represented through the following state equations:

$$\begin{cases} \dot{U} = -g \sin(\theta) + qw + (F_x + T)/m \\ \dot{w} = g \cos(\theta) - qU + F_z/m \\ \dot{q} = M_y/I_{yy} \\ \dot{\theta} = q \\ \dot{h} = U \sin(\theta) - w \cos(\theta), \end{cases}$$

where  $U, w$  are respectively the longitudinal and vertical body-axis velocity components,  $q$  is the pitch rate,  $\theta$  is the pitch angle,  $h$  is the altitude,  $F_x, F_z$  and  $M_y$  are the aerodynamic loads expressed in the body axis, and  $T$  is the total thrust force. Since the control problem concerns only the rotational dynamics of the aircraft,  $T$

is treated as a constant, leaving the elevator deflection as the sole control input.

Aerodynamic loads are expressed in the stability frame as functions of airspeed  $V = \sqrt{U^2 + w^2}$ , angle of attack  $\alpha = \arctan(w/U)$ , altitude  $h$ , and elevator deflection  $\delta$ :

$$\begin{aligned} F_x &= \frac{1}{2}\rho(h)V^2 S_{\text{ref}} C_x \\ F_z &= \frac{1}{2}\rho(h)V^2 S_{\text{ref}} C_z(\alpha, M, \delta) \\ M_y &= \frac{1}{2}\rho(h)V^2 S_{\text{ref}} d_{\text{ref}} C_m(\alpha, q, M, \delta). \end{aligned}$$

The lift and pitching-moment coefficients decompose into angle-of-attack and control-deflection terms:

$$\begin{aligned} C_z(\alpha, M, \delta) &= C_{z,\alpha}(\alpha, M) + C_{z,\delta}\delta \\ C_m(\alpha, q, M, \delta) &= C_{m,\alpha}(\alpha, M) + C_{m,q}q + C_{m,\delta}\delta. \end{aligned}$$

The baseline controller shown in Figure 3 is a cascaded structure with two outer proportional loops (commanding climb angle  $\gamma$  and vertical acceleration  $a_z$ ) and an inner loop INDI controlling the pitch rate. The outer-loop gains are kept equal to those in [3]; only the tuning of the inner-loop INDI is modified for the comparison of the controllers.

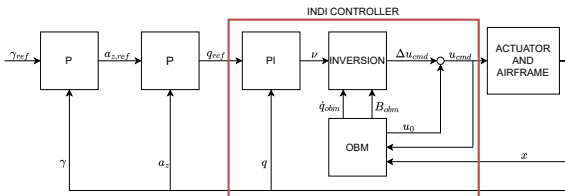


Figure 3: Structure of the cascaded autopilot with the inner loop INDI controller.

### 3.2. Controller design

Figure 4 shows the block diagram of the ESO-augmented INDI architecture designed for the longitudinal airframe model.

Sensor dynamics are approximated by first-order models that match their true cutoffs, which limits the control-loop bandwidth to 34 rad/s. Accordingly, the disturbance-rejection weight is set to this cutoff, while the tracking cutoff is set slightly lower to 15 rad/s.  $\mathcal{H}_\infty$  synthesis under these constraints yields the gains in Table 1.

As compared to [3], part of the control effort is delegated to the ESO.  $\mathcal{H}_\infty$  synthesis reduces the closed-loop bandwidth to account for the sensors. A lower integral gain is needed because

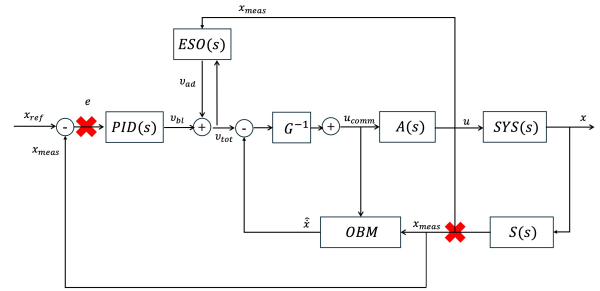


Figure 4: Block diagram of the inner loop architecture. Red crosses indicate where the loop is opened to compute stability margins.

Table 1: Controller tuning: sensors included vs baseline INDI.

Gain	ESO+INDI	Baseline INDI
$K_p$	9.648	18.5491
$K_i$	1.833	67.5795
$K_d$	0.006	–
$L_1$	54.052	–
$L_2$	362.149	–

the ESO architecture causes the INDI loop to act as a pure integrator.

The sensitivity functions of the ESO implementation, the baseline INDI, and the  $\mathcal{L}_1$  architecture of [3] are plotted in Figure 5. The ESO structure preserves most of the disturbance rejection capabilities of the  $\mathcal{L}_1$  while avoiding the sharp peak at the sensor bandwidth.

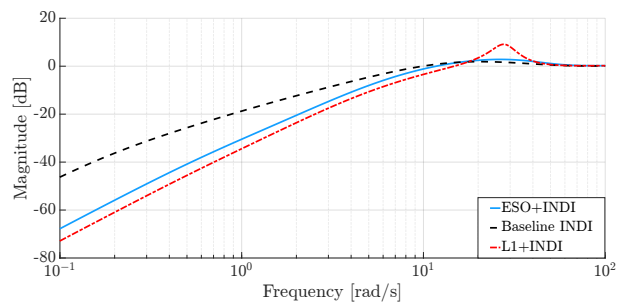


Figure 5: Sensitivity functions of baseline, ESO, and  $\mathcal{L}_1$  considering sensor dynamics.

### 3.3. Simulation results

When sensor dynamics is considered, stability margin analysis (Figure 6 and Table 2) shows that  $\mathcal{H}_\infty$  structured synthesis can tune the gains

of the ESO-INDI structure to increase either phase margin or bandwidth, if compared to the baseline INDI controller and the  $\mathcal{L}_1$ -INDI in [3].

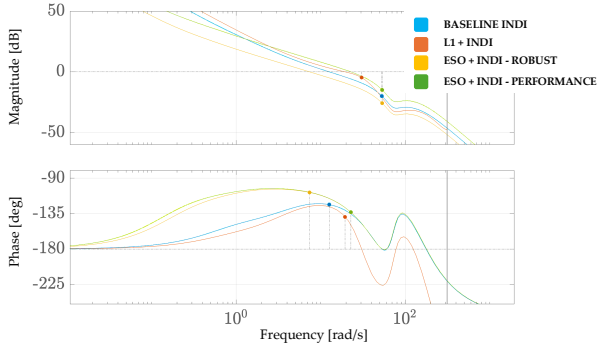


Figure 6: Bode diagram of the open-loop transfer function with sensor dynamics.

Par.	Base	L1	ESO-R	ESO-P
BW [rad/s]	12	19	7	22
PM [deg]	54	41	72	48
GM [dB]	23	4	26	18

Table 2: Performance and stability margins of the different controllers when sensor dynamics are included

With realistic sensor dynamics, model uncertainty, actuator degradation, and sinusoidal disturbance applied simultaneously, the ESO-augmented INDI controller maintains near-perfect tracking, effectively compensating for all perturbations. In contrast, the baseline INDI controller exhibits degraded performance and dangerous oscillations under the same conditions (Figure 7).

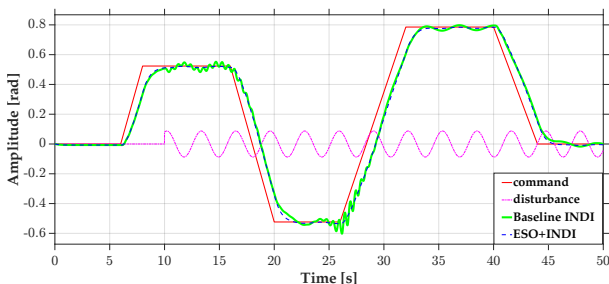


Figure 7: ESO-INDI vs Baseline INDI response with sensors active, sinusoidal disturbance, and modelling/actuator uncertainties.

To assess the ESO effectiveness, one compares the virtual disturbance, defined as  $\sigma = \nu_{bl} -$

$\dot{q}$ , and the ESO virtual disturbance estimate  $\hat{\sigma}$  (Figure 8).

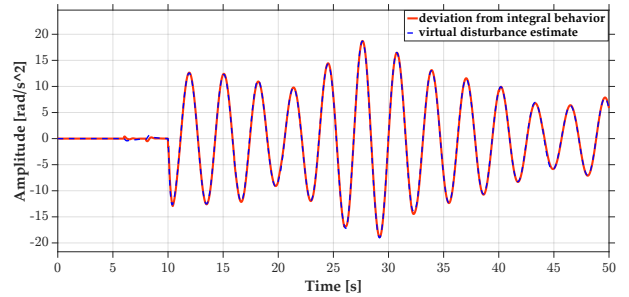


Figure 8: ESO tracking of the aggregate virtual disturbance

### 3.4. Under-estimated delay

Considering also a transport delay injected on the commanded input  $u$ , simulating CPU and transmission delay, stability margin analysis (Figure 9) shows again that  $\mathcal{H}_\infty$  structured synthesis can tune the gains of the ESO-INDI structure to increase either phase margin or bandwidth as compared to the baseline INDI controller and the  $\mathcal{L}_1$ -INDI in [3].

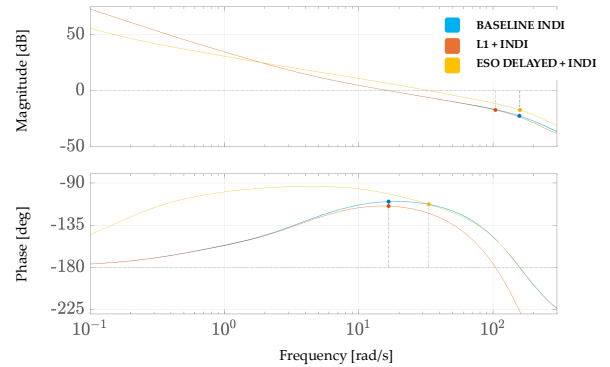


Figure 9: Bode diagram of the open-loop transfer function with transport delay.

When a 50 ms delay is underestimated as 30 ms in the ESO, command tracking remains satisfactory with only a slight lag in ramp response, showing robustness to delay inaccuracies. Performance degradation with respect to a delay-free system is marginal. For comparison, a classical Smith predictor architecture shows significant loss of robustness (Figure 10). The baseline INDI and the  $\mathcal{L}_1$ -INDI controller responses diverge to infinity, indicating instability. Equivalent results are obtained in the case of overestimation.

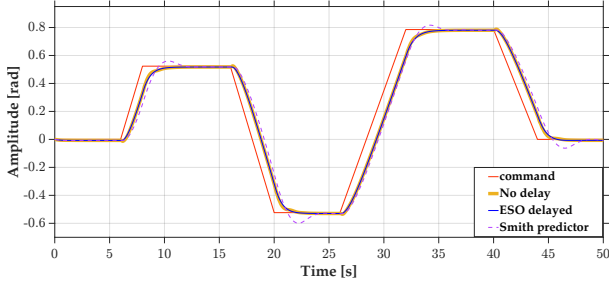


Figure 10: Smith-INDI and ESO-INDI with underestimated delay vs ESO-INDI delay-free time response. Sensor dynamics is active

### 3.5. Worst-case scenario

Under the combined worst-case scenario of low-frequency disturbance, model uncertainty, actuator degradation, sensor lag, and a 40 percent delay underestimation, the ESO-augmented controller still achieves satisfactory, controllable tracking, albeit with some residual error (Figure 11). Again, the baseline INDI and the  $\mathcal{L}_1$ -INDI controller responses diverge. The ESO still tracks the aggregate effect of the disturbance accurately (Figure 12).

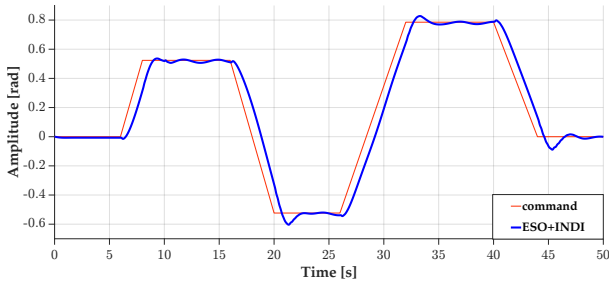


Figure 11: ESO+INDI response under worst-case perturbations and delay under-estimation.

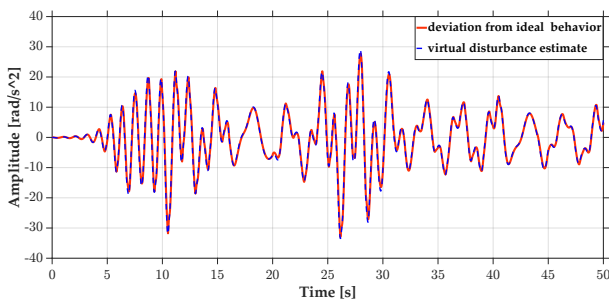


Figure 12: ESO tracking of the aggregate virtual disturbance with sensor dynamics active, underestimated delay, model uncertainties, and actuator degradation.

## 4. Conclusion and future developments

### 4.1. Results discussion

Validation on a longitudinal autopilot case study shows that the  $\mathcal{H}_\infty$ -tuned INDI-ESO controller surpasses the performance and stability margins of a classical INDI or  $\mathcal{L}_1$ -adaptive scheme when sensor phase lag or delay are present. The architecture is also robust to delay underestimation and reduces manual tuning effort.

### 4.2. Future research directions

Several promising extensions can build on this foundation. First, disturbance estimation could be improved by incorporating Gaussian radial basis functions or neural network hybrids within the ESO, providing richer function approximation capabilities. Second, online delay identification algorithms could be embedded in the control loop to adaptively refine the ESO's delay estimate under variable computational or transmission latencies. Finally, a natural progression is to extend the ESO-INDI framework to a multivariable flight control framework, developing vectorial disturbance observers and structured  $\mathcal{H}_\infty$  controllers that explicitly handle pitch-roll-yaw coupling, enabling a unified autopilot for both longitudinal and lateral-directional dynamics.

### 4.3. Aerospace industry impact

Since the feedback part of the control law is linear, powerful techniques such as  $\mathcal{H}_\infty$  approaches can be leveraged to compute the gains while satisfying performance and robustness requirements. The reduction of manual tuning effort makes INDI control more accessible to a broad range of aerospace platforms. Robustness to underestimated delays and sensor phase lag ensures reliable operation in perturbed flight conditions, while the minimal tuning overhead supports rapid deployment. In conclusion, this research lays the groundwork for incorporating adaptive INDI into next-generation autopilot systems.

## References

- [1] Y. Kumtepe, T. S. C. Pollack, and E. van Kampen. Flight control law design using hybrid incremental nonlinear dynamic inversion. In *AIAA SCITECH 2022 Forum*, San Diego, CA, 2022. American Institute of Aeronautics and Astronautics, AIAA. AIAA 2022-1597.
- [2] Ross J. Niewoehner, John T. Bosworth, William T. Bundick, and Eugene Lavretsky. Adaptive incremental nonlinear dynamic inversion control for an f-16 aircraft. In *AIAA Guidance, Navigation, and Control Conference*. American Institute of Aeronautics and Astronautics, 2015.
- [3] Giorgio Raos. Enhancing incremental ndi control with  $\mathcal{L}_1$  adaptive augmentation in a longitudinal autopilot. Master's thesis, Politecnico di Milano, Milan, Italy, 2024. Tesi di Laurea Magistrale in Aeronautical Engineering - Ingegneria Aeronautica.
- [4] S. Sieberling, Q. P. Chu, and J. A. Mulder. Robust flight control using incremental nonlinear dynamic inversion and angular acceleration prediction. *Journal of Guidance, Control, and Dynamics*, 33(6):1761–1772, November 2010.
- [5] R. C. van 't Veld. Incremental nonlinear dynamic inversion flight control: Stability and robustness analysis and improvements. Master's thesis, Delft University of Technology, Delft, The Netherlands, September 2016.